



HAL
open science

Plate bending, energetics of subduction and modeling of mantle convection: A boundary element approach

Gianluca Gerardi, Neil M. Ribe, Paul Tackley

► To cite this version:

Gianluca Gerardi, Neil M. Ribe, Paul Tackley. Plate bending, energetics of subduction and modeling of mantle convection: A boundary element approach. *Earth and Planetary Science Letters*, 2019, 515, pp.47-57. 10.1016/j.epsl.2019.03.010 . hal-02080175

HAL Id: hal-02080175

<https://hal.science/hal-02080175>

Submitted on 26 Mar 2019

HAL is a multi-disciplinary open access archive for the deposit and dissemination of scientific research documents, whether they are published or not. The documents may come from teaching and research institutions in France or abroad, or from public or private research centers.

L'archive ouverte pluridisciplinaire **HAL**, est destinée au dépôt et à la diffusion de documents scientifiques de niveau recherche, publiés ou non, émanant des établissements d'enseignement et de recherche français ou étrangers, des laboratoires publics ou privés.

Plate bending, energetics of subduction and modeling of mantle convection: a boundary element approach

Gianluca Gerardi^{a,*}, Neil M. Ribe^a, Paul J. Tackley^b

^a*Laboratoire FAST, University Paris-Sud, CNRS, Université Paris-Saclay, F-91405, Orsay, France*

^b*Institute of Geophysics, Department of Earth Sciences, ETH Zürich, Sonneggstrasse 5, 8092 Zürich, Switzerland*

Abstract

Several authors have suggested that mantle convection is primarily resisted by strong subduction zones, which if true implies small or even negative values of the exponent β in the Nusselt number/Rayleigh number relation $\text{Nu} \sim \text{Ra}^\beta$. To evaluate this hypothesis, we use the boundary element method (BEM) to study the energetics of subduction in a two-dimensional system comprising two purely viscous plates, a subducting plate (SP) and an overriding plate (OP), immersed in an infinitely deep ambient fluid beneath a free-slip surface. The negative buoyancy of the slab is the only driving force. The principal quantity of interest is the fraction R of the total viscous dissipation that occurs in the upper convective boundary layer comprising the SP, the OP and the subduction interface (SI) between them. Scaling analysis and BEM solutions of the instantaneous flow driven by an isolated SP yield $R \sim \text{St}/[\text{St} + F(\theta)]$, where St is the flexural stiffness of the SP and $F(\theta)$ is a function of the dip θ of the plate's leading edge. More realistic time-dependent solutions for the SP+OP case show that $R(t) \leq 0.4$ for reasonable viscosity contrasts $\eta_{\text{SP}}/\eta_{\text{ambient}} \in [250, 2500]$, indicating that the dissipation is dominated by the ambient mantle contribution. Finally, we formulate a parameterized model of mantle convection to evaluate the influence of subduction-zone dissipation on the effective value of

*Corresponding author

Email address: gianluca.gerardi@u-psud.fr (Gianluca Gerardi)

β , motivated by the possibility that the use of the classical value $\beta = 1/3$ in global parameterized convection models may be the cause of their failure to predict reasonable thermal histories. Using the correct length scale to describe bending (the ‘bending length’; Ribe (2010)), we find $\beta \in [0.25, 0.34]$, which is not much different than the classical result. We conclude that subduction zone dissipation is not large enough to change substantially the classical Nusselt number/Rayleigh number scaling law. It is therefore probably necessary to look elsewhere to reconcile geodynamical and geochemical arguments regarding the thermal history of the Earth.

1. Introduction

In the simplest terms, thermal convection in the mantle can be described as a Rayleigh-Bénard instability in the limit of infinite Prandtl number and high Rayleigh number (e.g Davaille & Limare, 2015). This type of convection
5 is associated with the scaling law

$$\text{Nu} \sim \text{Ra}^\beta \tag{1}$$

where $\text{Nu} = Q/Q_C$ (the Nusselt number) is the ratio between the total heat evacuated from the top of the convecting layer (Q) and the heat which would be transported by conduction alone (Q_C), while $\text{Ra} = g\rho\alpha\Delta TH^3/\kappa\eta$ (the Rayleigh
10 number) measures the vigor of convection in a fluid layer of thickness H across which a temperature difference ΔT is applied. The material properties ρ, α, κ , and η are, respectively, the density, thermal expansivity and diffusivity, and viscosity of the fluid and g is the gravitational acceleration. A critical parameter in (1) is the heat transfer scaling exponent β which quantifies the sensitivity
15 of the surface heat flow to variations of the vigor of convection. For an isoviscous fluid bounded by free-slip surfaces, steady-state boundary-layer analysis predicts $\beta = 1/3$ (e.g Turcotte & Schubert, 2014). However, if we exploit eq. (1) with $\beta = 1/3$ to build a parameterized cooling model for the Earth, the comparison between geological observations and the model predictions reveals

20 serious discrepancies. Indeed, geochemical and heat flow data for the present-day Earth indicate that the Urey ratio (Ur), defined as the ratio of radiogenic heat production to heat loss, is smaller than 0.50 (Stacey & Davis, 2008; Jaupart et al., 2015). On the contrary, parameterized cooling models with $\beta = 1/3$ suggest $Ur \approx 0.75$ (Jaupart & Mareschal, 2010; Labrosse & Jaupart, 2007). This
25 translates into an unrealistically high mantle temperature during the Archean obtained by backward time integration of the Earth's global energy budget.

One possible explanation for the mismatch between geochemical and geodynamical investigations lies in the high value $\beta = 1/3$ which makes the rate of secular cooling of the Earth highly sensitive to mantle temperature fluctuations (Christensen, 1985; Korenaga, 2003; Labrosse & Jaupart, 2007). This
30 means that one (or more) of the assumptions underlying the boundary-layer prediction might not be valid for mantle convection.

A characteristic element of mantle convection is the presence of a stiff lithosphere. Unlike the classical analysis in which the boundary layer is assumed
35 to have the same viscosity as the ambient fluid, the lithosphere is much stiffer than the underlying mantle. This fact inspired numerous investigations of thermal convection in a fluid with temperature-dependent viscosity, a feature that radically changes the style of convection (e.g. Nataf & Richter, 1982; Solomatov, 1995). However, if temperature-dependent viscosity is coupled with more
40 realistic interplate weak zones, the classical $Nu \sim Ra^{1/3}$ law is found to remain valid (Gurnis, 1989). A second crucial property of the terrestrial lithosphere that is not accounted for in classical boundary-layer theory is the generation of tectonic plates in relative movement. The most peculiar feature of the latter is one-sided subduction, whereby a highly viscous plate bends and slides along an
45 inclined subduction interface separating it from the overriding plate. The resistance to this deformation could strongly affect thermal convection by partially decoupling the dynamics of the lithosphere from the convection beneath it. The plate speed and the corresponding surface heat flow would then be less sensitive to any variations in the properties of the mantle, thereby reducing the effective
50 value of β .

This latter argument has been the object of considerable debate in the past 20 years and it is still unclear whether or not subduction dissipates a significant amount of energy (e.g. Irvine & Schellart, 2012; Leng & Zhong, 2010; Krien & Fleitout, 2008; Davies, 2009; Rose & Korenaga, 2011; Conrad & Hager, 1999b).

55 In the pioneering work of Conrad & Hager (1999a), the authors suggested that the bending of long and highly viscous plates at subduction zones dissipates most of the energy that drives mantle convection. On this view, the surface heat flux is nearly independent of the underlying mantle, implying $\beta \approx 0$ (Conrad & Hager, 1999b). A key parameter in the model of Conrad & Hager (1999a) is the

60 minimum radius of curvature \mathcal{R}_{\min} of the subducting plate, which the authors take to be 200 km. Subsequently, Korenaga (2003) proposed a counterintuitive scaling law with $\beta < 0$, implying that the surface heat flow decreases as mantle convection becomes more vigorous. According to Korenaga, the thickening of the lithosphere is controlled by dehydration during melting at mid-ocean ridges.

65 A hotter mantle (higher values of Ra), which produces more melt, would thus lead to a thicker lithosphere that slows down mantle convection. Davies (2009) compared two different mantle convection models in which the lithosphere thickens either by conductive cooling or by the dehydration stiffening process. He concluded that the result $\beta < 0$ is an artefact of the small value of $\mathcal{R}_{\min} = 200$

70 km and the high value of the SP viscosity $\eta_1 = 10^{23}$ Pa s assumed by Korenaga (2003). Higher values of $\mathcal{R}_{\min} = 300\text{-}500$ km and/or lower lithosphere viscosities ($\eta_1 = 10^{22}$ Pa s) recover the standard result $\beta = 1/3$ and imply that the dissipation of energy at subduction zones is minor. Other authors have suggested that the viscous dissipation associated with the deformation of the lithosphere

75 is never dominant. Using a numerical model for compressible convection, Leng & Zhong (2010) found that the dissipation occurring in a subduction zone is 10-20 % of the total dissipation. A slightly wider range, 10-30 %, is suggested by the study of Krien & Fleitout (2008), who combined analysis of short and intermediate wavelength gravity and geoid anomalies with the predictions of

80 a 2-D numerical model. Capitanio et al. (2007) investigated free subduction numerically using a constant or layered linear viscoelastic rheology and found

that the lithospheric dissipation is generally less than 25% of the total. Similar results are obtained when a plastic rheology is adopted to model the lithosphere (e.g. Buffett & Becker, 2012; Rose & Korenaga, 2011). This assumption seems
85 also to be consistent with observations arising from natural subduction zones concerning the relationship between subducting plate age and slab curvature (Buffett & Heuret, 2011; Holt et al., 2015).

In this study we investigate the energetics of subduction using a 2-D numerical model in which a subducting plate (SP) and an overriding plate (OP) interact
90 across a relatively weak interface. The model is dynamically self-consistent and the Stokes equations of motion are solved by means of the Boundary Element Method (BEM). Our investigation differs in two important ways from previous work. First, unlike numerous previous studies that look only at the deformation of the SP (e.g. Conrad & Hager, 1999b; Davies, 2009; Capitanio et al., 2007;
95 Irvine & Schellart, 2012), we explicitly quantify the deformation occurring in the subduction interface and the corresponding dissipation of energy. Second, we systematically interpret our results in the light of thin viscous-sheet theory (Ribe, 2001) to determine scaling laws that describe the physical mechanisms underlying our system.

100 The outline of the paper is as follows. After introducing the model setup and the BEM, we begin by performing a scaling analysis of instantaneous solutions of the Stokes equations for plates with a specified geometry. We find that the fraction R of the total energy dissipation that occurs in the upper convective boundary layer is controlled by three key parameters: the flexural
105 stiffness of the SP, the strength of the subduction interface and the shape (dip) of the descending slab. Next, we examine the time evolution of $R(t)$ during unsteady subduction of plates with medium/high viscosity. Time dependent solutions show that R remains always below 0.5, the value corresponding to equipartition of the dissipation between the boundary layer and the ambient
110 mantle. In conclusion, we explore the consequences of this result for the Nusselt number/Rayleigh number relationship $\text{Nu} \sim \text{Ra}^\beta$ for a convecting system with plates of moderate to high strength. A crucial result here is that the exponent

β can change dramatically depending on the length scale used to describe the dissipation due to bending of the SP. As demonstrated in Ribe (2010), the appropriate length scale is the ‘bending length’, which is the sum of the slab length
115 and the arcwise extent of the region of flexural bulging seaward of the trench. Adopting this length scale, we find $\beta \in [0.25, 0.34]$.

2. Model setup and BEM formulation

Figure 1 shows the initial geometry of our 2-D subduction model. The motion and deformation of the plates are entirely driven by the negative buoyancy of the descending slab, and the system is free of boundary constraints. The model comprises three fluids: i) an infinitely deep ambient mantle with viscosity η_0 and density ρ_0 , bounded above by a free-slip surface ($x_2=0$); ii) a subducting plate (SP) with viscosity $\eta_1 = \lambda_1\eta_0$ and density ρ_1 ; and iii) an overriding plate (OP) with viscosity $\eta_2 = \lambda_2\eta_0$ and density ρ_2 . The SP comprises a flat portion of length L_{SP} and an attached slab of length ℓ whose initial dip is θ_0 . The initial thickness h_{SP} of the SP is constant apart from the two rounded ends. The thickness and length of the OP are h_{OP} and L_{OP} , respectively. The rounded ends of the plates were designed to ensure continuity of curvature at all points along the contours C_1 and C_2 . A lubrication gap with initially constant thickness d_2 separates the SP from the OP. In each plate we define a midsurface located halfway between the upper and lower surfaces. The arclength coordinates along these surfaces are $s \in [0, L_{\text{SP}} + \ell]$ for the SP and $s_{\text{OP}} \in [0, L_{\text{OP}}]$ for the OP. Finally, above the plates is a lubrication layer of thickness d_1 that permits free horizontal motion of the plates. More details on the initial setup are given in § 2 of Gerardi & Ribe (2018).

The model of figure 1 represents a Stokes flow problem with deformable fluid/fluid interfaces. Such problems can be solved efficiently using the Boundary-Element Method (BEM), a numerical technique based on the boundary-integral representation of Stokes flow. For the geometry of figure 1, that representation yields the following integral equation for the fluid velocity (Manga & Stone, 1993; Pozrikidis, 1992):

$$\begin{aligned}
& \chi_0(\mathbf{x})\mathbf{u}^{(0)}(\mathbf{x}) + \chi_1(\mathbf{x})\lambda_1\mathbf{u}^{(1)}(\mathbf{x}) + \chi_2(\mathbf{x})\lambda_2\mathbf{u}^{(2)}(\mathbf{x}) \\
&= \frac{\Delta\rho_1}{\eta_0} \int_{C_1} (\mathbf{g}\cdot\mathbf{y})\mathbf{n}(\mathbf{y})\cdot\mathbf{J}(\mathbf{y}-\mathbf{x})d\ell(\mathbf{y}) + \\
&+ \frac{\Delta\rho_2}{\eta_0} \int_{C_2} (\mathbf{g}\cdot\mathbf{y})\mathbf{n}(\mathbf{y})\cdot\mathbf{J}(\mathbf{y}-\mathbf{x})d\ell(\mathbf{y}) + \\
&+ (1-\lambda_1) \int_{C_1} \mathbf{u}^{(1)}(\mathbf{y})\cdot\mathbf{K}(\mathbf{y}-\mathbf{x})\cdot\mathbf{n}(\mathbf{y})d\ell(\mathbf{y}) + \\
&+ (1-\lambda_2) \int_{C_2} \mathbf{u}^{(2)}(\mathbf{y})\cdot\mathbf{K}(\mathbf{y}-\mathbf{x})\cdot\mathbf{n}(\mathbf{y})d\ell(\mathbf{y}). \tag{2}
\end{aligned}$$

In (2), $\mathbf{u}^{(i)}(\mathbf{x})$ ($i = 0, 1$ or 2) is the velocity of the fluid at the point $\mathbf{x} \in A_i$, where A_i is the domain occupied by fluid i . The density differences are $\Delta\rho_i = (\rho_i - \rho_0)$, and $\mathbf{n}(\mathbf{y})$ is the unit vector normal to the contour C_1 or C_2 that points out of the plate. The coefficients $\chi_i(\mathbf{x})$ for $i = 1$ and 2 have the values 0 , $1/2$ or 1 if $\mathbf{x} \notin A_i$, $\mathbf{x} \in C_i$ or $\mathbf{x} \in A_i$, respectively. The coefficient $\chi_0(\mathbf{x})$ is 0 for $\mathbf{x} \notin A_0$, $1/2$ for $\mathbf{x} \in C_1 \vee \mathbf{x} \in C_2$ and 1 for $\mathbf{x} \in A_0$. $\mathbf{J}(\mathbf{y}-\mathbf{x})$ and $\mathbf{K}(\mathbf{y}-\mathbf{x})$ are singular solutions (Green functions) of the Stokes equation for the velocity and the stress, respectively, at the point \mathbf{y} due to a line force at \mathbf{x} . To prepare eq. (2) for solution, we first write it in terms of dimensionless (hatted) variables

$$(\hat{\mathbf{x}}, \hat{\mathbf{y}}) = h_{\text{SP}}^{-1}(\mathbf{x}, \mathbf{y}), \quad \hat{\mathbf{u}}^{(i)} = \frac{\eta_0}{h_{\text{SP}}^2 g \Delta\rho_1} \mathbf{u}^{(i)} \quad (i = 0, 1, 2). \tag{3}$$

Next, (2) is written as two coupled integral equations for the velocities on the interfaces C_1 and C_2 by setting $\mathbf{x} \in C_1$ and $\mathbf{x} \in C_2$ and choosing the appropriate values of χ_0 , χ_1 and χ_2 for each case. The integral equations are then solved using the procedure described by Gerardi & Ribe (2018). Once the interfacial velocities are known, the velocity at points \mathbf{x} away from the interfaces can be computed by choosing the appropriate values of $\chi_0(\mathbf{x})$, $\chi_1(\mathbf{x})$ and $\chi_2(\mathbf{x})$ and then evaluating the integrals in (2). Finally, for time-dependent solutions the interfacial points are advanced by solving

$$\frac{d\hat{\mathbf{x}}}{d\hat{t}} = \hat{\mathbf{u}}(\hat{\mathbf{x}}), \quad \hat{t} = \frac{h_{\text{SP}} g \Delta\rho_1}{\eta_0} t, \tag{4}$$

where \hat{t} is the dimensionless time. More details on the BEM formulation are
170 given in § 3 of Gerardi & Ribe (2018).

3. Rates of viscous dissipation of energy

The main goal of this work is to quantify the amount of energy dissipated in a subduction zone and to understand how that dissipation is partitioned among the different elements of the system. Accordingly, we write the total dissipation rate D_{Total} as a sum of four contributions, viz.,

$$D_{\text{Total}} = D_{\text{SP}} + D_{\text{OP}} + D_{\text{SI}} + D_{\text{M}} \quad (5)$$

where the terms on the right-hand side represent the rates of viscous dissipation due to the deformation of the subducting plate (D_{SP}), the overriding plate (D_{OP}), the subduction interface (D_{SI}) and the ambient mantle (D_{M}).

Consider first the total dissipation rate D_{Total} . The balance of mechanical energy for a 2D Stokes flow in an area A bounded by a contour C is

$$2\eta \int_A e_{ij} e_{ij} dA = \int_C u_i \sigma_{ij} n_j d\ell + \int_A u_j f_j dA. \quad (6)$$

Eq. (6) states that the total rate of dissipation in an area A (left-hand side) is the sum of the rate at which the fluid stress σ_{ij} does work on C (first term on the right-hand side) plus the rate at which the gravitational body force $f_j = -\rho g \delta_{j3}$ does work on A (second term). Now introduce the modified pressure $\bar{p} = p + \rho g x_3$ and the corresponding modified stress tensor $\bar{\sigma}_{ij} = -\bar{p} \delta_{ij} + 2\eta e_{ij} = \sigma_{ij} - \rho g x_3 \delta_{ij}$. Eq. (6) then takes the simpler form

$$2\eta \int_A e_{ij} e_{ij} dA = \int_C u_i \bar{\sigma}_{ij} n_j d\ell, \quad (7)$$

which states that the total rate of viscous dissipation in A is equal to the rate at which the modified stress performs work on C . For the three-fluid domain with a free-slip upper surface shown in figure 1,

$$D_{\text{M}} + D_{\text{SI}} = \int_{C_1} u_i \bar{\sigma}_{ij}^{(0)} (-n_j) d\ell + \int_{C_2} u_i \bar{\sigma}_{ij}^{(0)} (-n_j) d\ell, \quad (8a)$$

$$D_{\text{SP}} = \int_{C_1} u_i \bar{\sigma}_{ij}^{(1)} n_j d\ell, \quad D_{\text{OP}} = \int_{C_2} u_i \bar{\sigma}_{ij}^{(2)} n_j d\ell, \quad (8b)$$

where $\bar{\sigma}_{ij}^{(i)}$ ($i=0,1$ or 2) is the modified stress tensor of fluid i . The quantity $-n_j$ appears in (8a) because the normal vector that points out of the area

A_0 is opposite to \mathbf{n} , which was defined as pointing out of the plates. Now substitute eq. (8) into eq. (5) and apply the normal stress matching conditions
 200 $(\bar{\sigma}_{ij}^{(k)} - \bar{\sigma}_{ij}^{(0)})n_j = n_i\Delta\rho_kgy_j$ for points on C_k ($k = 1$ or 2). The result is

$$D_{\text{Total}} = \Delta\rho_1g \int_{C_1} u_i n_i y_j d\ell + \Delta\rho_2g \int_{C_2} u_i n_i y_j d\ell. \quad (9)$$

Because we know (i.e., have calculated) the velocity \mathbf{u} on C_1 and C_2 , (9) implies that the total dissipation rate can be obtained simply by evaluating two integrals over the fluid/fluid interfaces. In this study, however, we shall assume a neutrally
 205 buoyant OP ($\Delta\rho_2 = 0$), whereupon the second integral in (9) vanishes.

We now turn to the dissipation rates D_{SP} and D_{OP} within the two plates. In principle these could be calculated from (7). However, determination of the stress $\bar{\sigma}_{ij}$ on C_1 and C_2 requires the solution of Fredholm integral equations of the first kind, which are notorious for their numerical instability. Accordingly,
 210 we exploit thin viscous-sheet theory (Ribe, 2001) to write

$$D_{\text{SP}} = \int_0^{L_{\text{SP}}+\ell} \left(4\eta_1 h_{\text{SP}} \Delta^2 + \frac{1}{3}\eta_1 h_{\text{SP}}^3 \dot{K}^2 \right) ds, \quad (10a)$$

$$D_{\text{OP}} = \int_0^{L_{\text{OP}}} \left(4\eta_2 h_{\text{OP}} \Delta^2 + \frac{1}{3}\eta_2 h_{\text{OP}}^3 \dot{K}^2 \right) ds, \quad (10b)$$

where Δ is the rate of stretching of the midsurface of the sheet, \dot{K} is its rate
 215 of change of curvature, and s is the arclength along it. The total rate of dissipation within each plate is thus the sum of contributions from deformation by stretching/shortening ($4\eta h \Delta^2$) and by bending ($1/3\eta h^3 \dot{K}^2$). The quantities Δ and \dot{K} are calculated by numerical differentiation of the velocity \mathbf{u} on the sheet's midsurface (Ribe, 2010; Gerardi & Ribe, 2018).

220 Next, we calculated the rate of viscous dissipation within the SI from the integral

$$D_{\text{SI}} = 2\eta_0 \int_{A_{\text{SI}}} e_{ij} e_{ij} dA_{\text{SI}} \quad (11)$$

where A_{SI} is the area of the fluid in the lubrication gap between the plates. We evaluated the integral (11) by assuming that the fluid velocity varies linearly
 225 across the gap between the known values on either side.

Finally, the rate of viscous dissipation in the ambient mantle (D_M) is obtained from eq.(5) once all the other quantities are known.

4. Scaling analysis

In this section we determine the crucial dimensionless parameters that control the energetics of subduction by performing a scaling analysis of instantaneous BEM solutions. Because inertia is negligible in Stokes flow, the energetic state of the system at any instant is fully determined by the geometry of the plates at that instant. Time is therefore a mere parameter, which we here ignore by focussing on the instantaneous geometry shown in figure 1.

As a target parameter for our scaling analysis, we define the ‘dissipation ratio’ R

$$R = \frac{D_{\text{SP}} + D_{\text{OP}} + D_{\text{SI}}}{D_{\text{Total}}} \equiv \frac{D_{\text{BL}}}{D_{\text{Total}}}. \quad (12)$$

R is the fraction of the total energy dissipation that occurs in the upper convective boundary layer comprising the two plates plus the SI.

4.1. Subduction of an isolated SP

For simplicity we begin by considering the subduction of an isolated SP without an OP or a SI, for which $D_{\text{BL}} \equiv D_{\text{SP}}$. We call this the SP ONLY case.

Looking at figure 1, we can see that the portion of the SP that deforms by bending is characterized by the length ℓ_b (bending length), which is the sum of the length ℓ of the slab and the width ℓ_{fb} of the region seaward of the trench where flexural bulging occurs (Ribe, 2010). If the SP sinks with a characteristic speed V_{Sink} , its rate of change of curvature scales as $\dot{K} \sim V_{\text{Sink}}/\ell_b^2$. Neglecting the dissipation due to stretching and integrating over the bending length, we see that (10a) implies

$$D_{\text{SP}} \sim \eta_1 h_{\text{SP}}^3 \left(\frac{V_{\text{Sink}}^2}{\ell_b^3} \right) f_1(\theta). \quad (13)$$

The unknown function $f_1(\theta)$ accounts for the influence of the shape of the midsurface of the SP on the slab’s sinking speed (Ribe, 2010). A dip-dependency of D_{SP} is also in agreement with the results of Rose & Korenaga (2011). Apart from the factor $f_1(\theta)$, eq.(13) differs from analogous expressions in previous studies (e.g. Conrad & Hager, 1999a; Buffett, 2006; Capitanio et al., 2009) by

the presence of the characteristic bending length scale ℓ_b instead of \mathcal{R}_{\min} . Next, we estimate the total dissipation rate in the ambient mantle by scaling (6). This yields

$$D_M \sim \eta_0 V_{\text{Sink}}^2 f_2(\theta), \quad (14)$$

260 which is obtained using the scales $e_{ij} \sim V_{\text{Sink}}/\ell_b$ and $A_0 \sim \ell_b^2$. Like (13), it contains an unknown function $f_2(\theta)$.

Now because $D_{\text{BL}} = D_{\text{SP}}$ and $D_{\text{Total}} = D_{\text{SP}} + D_M$, equations (13), (14) and (12) imply

$$R \sim \frac{\text{St}}{\text{St} + \text{F}(\theta)}, \quad (15)$$

265 where $\text{F}(\theta) = f_2(\theta)/f_1(\theta)$ and $\text{St} \equiv (\eta_1/\eta_0) (h_{\text{SP}}/\ell_b)^3$ is the flexural stiffness of the SP that measures its mechanical resistance to bending (Ribe, 2010).

Let us now test the scaling law (15) against our BEM solutions. To do this, we run a large number of models for three values of θ_0 and different values of ℓ/h_{SP} , $L_{\text{SP}}/h_{\text{SP}}$ and $\lambda_1 \equiv \eta_1/\eta_0$, computing for each case the flexural stiffness 270 St and the dissipation number R . The results are shown in figure 2. The solid symbols show results for which the bending contribution to D_{SP} exceeds 95%. These collapse onto three master curves, one for each value of θ_0 , thereby confirming the scaling law (15). In the limit of $\text{St} \gg 1$, where we can suppose $\text{St} \gg \text{F}(\theta_0)$, R tends to a constant value that is independent of θ_0 , as expected 275 from eq. (15). Open symbols, shown for completeness, are for models with a significant ($\geq 5\%$) stretching contribution to D_{SP} , and which for that reason obey less well the scaling law (15).

The three master curves in figure 2 highlight two other interesting features. First, they tell us something about the temporal evolution of the system. In 280 particular, the curves show that R increases if either St or θ_0 increases. Now, during unsteady subduction, St decreases because the slab length increases, whereas θ_0 increases because the slab gets steeper. We therefore expect the system to evolve as indicated by the thick green arrow. We will verify this later during our analysis of time-dependent BEM solutions. Second, the curves show 285 that R never exceeds 0.7 and is typically < 0.5 . The latter value represents the

'equipartition limit', where the dissipation is equally shared between the mantle and the plate. Only stiff plates exceed this limit.

4.2. Subduction below an OP

We now add the OP to the system. For this SP+OP case, $D_{\text{BL}} \equiv D_{\text{SP}} +$
 290 $D_{\text{OP}} + D_{\text{SI}}$. We expect the OP to have two opposite effects on the dissipation ratio. On the one hand, it should increase R because deformation of the subduction interface and of the OP itself leads to higher dissipation within the boundary layer. On the other hand, the OP acts as a no-slip boundary condition on the mantle fluid below, enhancing the dissipation in that region and
 295 decreasing R . The inset of figure 3 shows a close-up view of the subduction interface (lubrication gap), which has thickness d_2 , inclination angle θ_{SI} , and viscosity η_{SI} . Assuming that layer-parallel shear in the gap gives the largest contribution to viscous dissipation, we use (11) to scale D_{SI} as

$$D_{\text{SI}} \sim \eta_{\text{SI}} V_{\text{Conv}}^2 \left(\frac{h_{\text{SP}}}{d_2} \right) (\sin\theta_{\text{SI}})^{-1}, \quad (16)$$

300 where V_{Conv} is the convergence speed of the descending slab. In writing (16), we have assumed that $e_{ij} \sim V_{\text{Conv}}/d_2$ and $A_{\text{SI}} \sim d_2 h_{\text{SP}}/\sin(\theta_{\text{SI}})$. We defined V_{Conv} to be the tangential component of the velocity vector on the SP's midsurface where it intersects the depth $x_2 = -h_{\text{SP}} - d_1$ (see inset of figure 3). To verify (16), we compare it with the predictions of a large number of BEM solutions
 305 that include an OP. For this purpose, we rewrite (16) in dimensionless form as

$$\hat{D}_{\text{SI}} \sim \gamma \hat{V}_{\text{Conv}}^2 (\sin\theta_{\text{SI}})^{-1}, \quad (17)$$

where

$$\hat{D}_{\text{SI}} = \frac{\eta_0}{h_{\text{SP}}^4 (g\Delta\rho_1)^2} D_{\text{SI}}, \quad \hat{V}_{\text{Conv}} = \frac{\eta_0}{h_{\text{SP}}^2 g\Delta\rho_1} V_{\text{Conv}}, \quad \gamma = \frac{\eta_{\text{SI}}}{\eta_0} \frac{h_{\text{SP}}}{d_2}. \quad (18)$$

The quantity γ is the dimensionless strength of the SI (Gerardi & Ribe, 2018).
 310 Because $\eta_{\text{SI}} = \eta_0$ in our model, we explore the influence of γ by varying d_2 alone (Gerardi & Ribe, 2018). Figure 3 shows \hat{D}_{SI} , computed numerically using eq. (11), as a function of $\gamma \hat{V}_{\text{Conv}}^2 (\sin\theta_{\text{SI}})^{-1}$ for 108 BEM solutions for the ranges of parameters given in the caption of figure 3. All the points collapse onto a straight line with slope of unity, confirming the scaling law (17).

315 Turning now to the rate of dissipation within the OP, our BEM solutions show that the energy dissipated to deform the OP is never more than $0.03D_{\text{BL}}$, whatever system configuration we use. We can therefore safely assume $D_{\text{BL}} \approx D_{\text{SP}} + D_{\text{SI}}$ for our SP+OP case study.

A natural next step would be to determine a complete scaling law for R that
320 includes the effect of the SI and that reduces to (15) in the limit $\gamma = 0$ of an infinitely weak (i.e., thick) SI. However, this turns out to be impractical given the large number of parameters involved. Instead, we show in figure 4 how the value of γ influences the dissipation ratio R . Dissipation in the SI can enhance R significantly, but only for low values of the SP's flexural stiffness ($\text{St} \ll 1$).
325 In this limit, D_{SI} can exceed D_{SP} by a factor of two or more. However, as soon as St increases beyond ≈ 2 , the effect of γ vanishes and we recover to a good approximation the corresponding SP ONLY case (empty circles in figure 4). Moreover, in the limit $\gamma \rightarrow 0$ we recover the SP ONLY results for all values of the stiffness St , whereas when $\gamma > 6$ the curves saturate and R does not change
330 anymore (data not shown to save space).

5. Time-evolving subduction

Our next task is to explore how R varies during unsteady subduction, focussing on the more realistic SP+OP case. We consider two examples: ‘low viscosity contrast’, with $\lambda_1 = 250$ and ‘high viscosity contrast’, with $\lambda_1 = 2500$.
335 The remaining parameters for both examples are given in table 1.

We ran the simulations until the slab’s tip reached the depth $x_2 = -6.7h_{\text{SP}}$, keeping track of $R(t)$ and $\text{St}(t)$. The results are shown in figure 5 for $\lambda_1 = 250$ (top) and $\lambda_1 = 2500$ (bottom). Figures 5a and 5c show the geometry of the system at three characteristic times. Figures 5b and 5d show the corresponding
340 time evolution of $R(t)$ as a function $\text{St}(t)$ (black filled circles). Time increases from right to left along these curves. The fraction $D_{\text{SI}}/D_{\text{BL}}$ of the boundary-layer dissipation that occurs in the SI is also noted for the three times. Finally, the green open circles show $R(\text{St})$ for the same SP but without the OP.

The first important result of figure 5 is that R remains always below the value
345 0.5 that corresponds to equipartition of the dissipation between the boundary layer and the ambient mantle. Second, the shapes of the curves concerning the subduction of an isolated SP (figure 5b and d, green empty circles), which show R increasing as St decreases and θ increases, agree with what we expected from our earlier SP ONLY solutions (Figure 2, § 4.1). The behavior of the SP+OP
350 case is more complex (figure 5b and d, black filled circles). Recall that the temporal evolution of R reflects a balance between two competing effects: a dynamical one (R decreases as St and $D_{\text{SI}}/D_{\text{BL}}$ decrease with time) and a geometrical one (R increases as the slab dip increases). For the SP+OP case with $\lambda_1 = 250$, the dynamical effect dominates at first, leading to a steady decrease
355 of R with time. Then, at $\text{St} \approx 0.6$, the balance is reversed and R starts to increase (figure 5b). For $\lambda_1 = 2500$, by contrast, the two effects nearly cancel out, maintaining a constant value $R \approx 0.4$ (figure 5d). Interestingly, for both cases, the relative importance of the dissipation at the interface ($D_{\text{SI}}/D_{\text{BL}}$) decreases as subduction proceeds. Indeed, BEM solutions show that both D_{SI} and D_{BL}
360 increase with time, but the latter increases faster so that at one point it starts

to dominate the overall dissipation within the boundary layer. Nevertheless, at the end of the simulations, D_{SI} is still significant: 44% and 34% of D_{BL} for $\lambda_1 = 250$ and $\lambda_1 = 2500$, respectively.

Finally, we note that for $\lambda_1 = 2500$ the simulations for the SP+OP and the
365 SP ONLY cases have rather similar variations of R as a function of $St \in [2, 10]$. This agrees with the results of figure 4, which show that the influence of the OP on the energetics of the system becomes almost negligible for $St > 2$. This is not the case for $\lambda_1 = 250$, for which the SP+OP and the SP ONLY simulations follow very different paths in the St - R space.

370 **6. Parameterized model of mantle convection**

Inspired by the approach of Conrad & Hager (1999b), we now construct a parameterized convection model by considering steady-state thermal convection in a cell of length L_h and thickness H (figure 6). At the top of cell is the SP which thickens by conductive cooling as it moves toward the trench, reaching a thickness h_{SP} when it enters the subduction zone. We assume no heat sources within the system and we consider a well-mixed mantle (i.e. high mantle Rayleigh numbers, Ra_m) at temperature T_m . The only temperature difference is across the SP, and is $\Delta T = T_m - T_{\text{Surf}}$, where T_{Surf} is the temperature at the SP's surface.

380 We begin by defining the Nusselt number (Nu) of the convecting cell as the ratio of the surface heat flow in the presence of convection to that transported purely by conduction (e.g. Turcotte & Schubert, 2014). The numerator is the integral over the length L_h of the vertical temperature gradient predicted by the standard half-space cooling model. The denominator is the heat transported by conduction across the entire thickness of the cell H . We thus have

$$\text{Nu} = 2H \left(\frac{U_{\text{SP}}}{\pi\kappa L_h} \right)^{1/2}, \quad (19)$$

where κ is the thermal diffusivity and U_{SP} is the horizontal speed of the SP. Scaling the continuity equation in the convecting cell, we obtain

$$\frac{U_{\text{SP}}}{L_h} \sim \frac{V_{\text{Sink}}}{L_z} \quad (20)$$

390 where L_z is the vertical distance from the slab's tip to the lower surface of the SP (figure 6). Equation (20) allows us to rewrite (19) as

$$\text{Nu} \sim H \left(\frac{V_{\text{Sink}}}{\kappa L_z} \right)^{1/2}. \quad (21)$$

The next step is to determine V_{Sink} in terms of the different contributions to the viscous dissipation at the subduction zone. The global balance of mechanical energy is

$$D_M + D_{\text{BL}} \equiv D_M(1 + \hat{R}) \sim h_{\text{SP}} \ell g \Delta \rho_1 V_{\text{Sink}}, \quad (22)$$

where $D_{\text{BL}} \sim \hat{R}D_{\text{M}}$, $\hat{R} \equiv R/(1 - R)$, and $D_{\text{Total}} \sim h_{\text{SP}}\ell g\Delta\rho_1 V_{\text{Sink}}$. Making use of (14) for D_{M} , we obtain

$$V_{\text{Sink}} \sim \frac{h_{\text{SP}}\ell g\Delta\rho_1}{\eta_0 f_2(\theta)(1 + \hat{R})}. \quad (23)$$

400 Because (23) relates the slab's sinking speed to the coefficient \hat{R} that describes the partitioning of viscous dissipation between the boundary layer and the mantle, we expect different regimes of mantle convection depending on the value of \hat{R} .

6.1. Thermal convection dominated by mantle viscous dissipation

405 In this subsection we recover the well-known result for the Nusselt number predicted by boundary-layer analysis of an isoviscous system. Here the energy dissipated to deform the lithosphere is negligible (i.e. $D_{\text{M}} \gg D_{\text{BL}}$ and $\hat{R} \rightarrow 0$). The thickness of the lithosphere h_{SP} is given by the half-space cooling model as

$$410 \quad h_{\text{SP}} \sim \left(\frac{\kappa L_h}{U_{\text{SP}}} \right)^{1/2}. \quad (24)$$

Substituting (20) and (23) into (24), we obtain

$$\frac{h_{\text{SP}}}{H} \sim \left(\frac{L_z f_2(\theta)}{\ell \text{Ra}_m} \right)^{1/3}, \quad (25)$$

where the Rayleigh number of the entire cell is $\text{Ra}_m \equiv H^3 g\Delta\rho_1 / (\kappa\eta_0)$. Then substituting (23) into (21) and using (25), we obtain

$$415 \quad \text{Nu} \sim \text{Ra}_m^{1/3} \left(\frac{\ell}{L_z f_2(\theta)} \right)^{1/3}, \quad (26)$$

which is the standard Nusselt number vs. Rayleigh number scaling for an isoviscous system.

Our next task is to understand what happens when $\hat{R} \neq 0$.

6.2. Thermal convection below a strong deforming boundary layer

420 From the definition $\hat{R} = D_{\text{BL}}/D_{\text{M}}$, we observe that

$$\hat{R} \sim \frac{\eta_1}{\eta_0} \left(\frac{h_{\text{SP}}}{\ell_b} \right)^3 F(\theta) + \frac{\eta_{\text{SI}}}{\eta_0} \left(\frac{h_{\text{SP}}}{d_{\text{SI}} \sin(\theta_{\text{SI}}) f_2(\theta)} \right) \left(\frac{V_{\text{Conv}}}{V_{\text{Sink}}} \right)^2, \quad (27)$$

where we have used (13), (14) and (16) to scale the different contributions to the viscous dissipation. Substituting (27) into (23) we obtain a nonlinear implicit equation for the sinking speed of the slab:

$$V_{\text{Sink}} \sim \frac{h_{\text{SP}} \ell g \Delta \rho_1}{\eta_0 f_2(\theta)} \left[1 + \frac{\eta_1}{\eta_0} \left(\frac{h_{\text{SP}}}{\ell_b} \right)^3 F(\theta) + \frac{\eta_{\text{SI}}}{\eta_0} \left(\frac{h_{\text{SP}}}{d_{\text{SI}} \sin(\theta_{\text{SI}}) f_2(\theta)} \right) \left(\frac{V_{\text{Conv}}}{V_{\text{Sink}}} \right)^2 \right]^{-1}. \quad (28)$$

Following Conrad & Hager (1999b), we define two additional Rayleigh numbers for the SP and the SI:

$$\text{Ra}_{\text{SP}} \equiv \frac{\ell_b^3 g \Delta \rho_1}{\kappa \eta_1}, \quad \text{Ra}_{\text{SI}} \equiv \frac{d_{\text{SI}}^3 g \Delta \rho_1}{\kappa \eta_{\text{SI}}}. \quad (29)$$

These Rayleigh numbers measure the importance of viscous dissipation within the SP and the SI relative to the energy available within the system. They become large in the limits $D_{\text{SP}} \rightarrow 0$ and/or $D_{\text{SI}} \rightarrow 0$ for fixed h_{SP} , which limits correspond to decreasing viscosity (η_1 or η_{SI}) and/or increasing length scale (ℓ_b or d_2). In terms of these Rayleigh numbers, (28) can be written as

$$V_{\text{Sink}} \sim \text{Ra}_{\text{m}} \frac{h_{\text{SP}} \ell \kappa}{f_2(\theta) H^3} \times \left[1 + \frac{\text{Ra}_{\text{m}}}{\text{Ra}_{\text{SP}}} \left(\frac{h_{\text{SP}}}{H} \right)^3 F(\theta) + \frac{\text{Ra}_{\text{m}}}{\text{Ra}_{\text{SI}}} \left(\frac{h_{\text{SP}}}{H} \right) \left(\frac{d_{\text{SI}}^2}{H^2 \sin(\theta_{\text{SI}}) f_2(\theta)} \right) \left(\frac{V_{\text{Conv}}}{V_{\text{Sink}}} \right)^2 \right]^{-1}. \quad (30)$$

We now investigate two limiting cases of (30).

6.2.1. Case 1: convection beneath a plate with a short travel time

Consider first the case of a lithosphere that moves from the ridge to the trench in a time $t = L_h/U_{\text{SP}} < 80$ Myr, the age at which seafloor flattening is observed to begin (e.g. Sclater et al., 1980; Conrad & Hager, 1999b). This implies that h_{SP} increases continually according to the half-space cooling model. Suppose initially that the viscous dissipation in the subduction interface is negligible ($\text{Ra}_{\text{SI}} \rightarrow \infty$). Simplifying (30) accordingly and substituting eq. (20) and

eq. (30) in eq. (24), we find

$$\frac{h_{\text{SP}}}{H} \sim \left(\frac{\text{Ra}_{\text{SP}}}{\text{Ra}_{\text{m}}} \frac{L_z f_2(\theta)}{\text{Ra}_{\text{SP}} \ell - f_1(\theta) L_z} \right)^{1/3}. \quad (31)$$

Now using (31) and the simplified form of (30) in eq. (21) we obtain

$$\text{Nu} \sim \left(\frac{\ell}{L_z f_2(\theta)} - \frac{F(\theta)}{\text{Ra}_{\text{SP}}} \right)^{1/3} \text{Ra}_{\text{m}}^{1/3}. \quad (32)$$

450 The Nusselt number still scales as $\text{Ra}_{\text{m}}^{1/3}$, but the prefactor decreases as the dissipation rate within the SP increases (i.e., as Ra_{SP} decreases). This result remains valid as long as the denominator of (31) is nonzero, i.e., if $\text{Ra}_{\text{SP}} \gg f_1(\theta) L_z / \ell$. This condition follows from the fact that when Ra_{SP} decreases the convection progressively slows down, increasing the traveling time of the litho-
455 sphere. Because the lithosphere then has more time to thicken, Ra_{SP} decreases even further, triggering a positive feedback that leads to an unphysical infinite plate thickness (Conrad & Hager, 1999b).

To understand the influence of viscous dissipation in the SI, we adopt (30) in its full form. Following again the steps in § 6.1 and assuming $\text{Ra}_{\text{SP}} \gg f_1(\theta) L_z / \ell$,
460 we obtain

$$\left(\frac{h_{\text{SP}}}{H} \right)^3 - \left(\frac{h_{\text{SP}}}{H} \right) \left(\frac{d_{\text{SI}}^2}{H^2} \frac{\mathcal{A}_1}{\text{Ra}_{\text{SI}}} \right) \sim \left(\frac{\mathcal{A}_2}{\text{Ra}_{\text{m}}} \right), \quad (33)$$

where $\mathcal{A}_1 \equiv C_V^2 (L_z / \ell) / \sin \theta_{\text{SI}}$, $\mathcal{A}_2 \equiv (L_z / \ell) f_2(\theta)$ and $C_V \equiv V_{\text{Conv}} / V_{\text{Sink}}$. Our BEM simulations show that C_V is always less than unity, and we treat it here as a constant. Obtaining representative values of \mathcal{A}_1 and \mathcal{A}_2 from our BEM
465 solutions, we solve (33) numerically for $\text{Ra}_{\text{SI}}(d_2, \eta_{\text{SI}}) \leq 0.4$ and $\text{Ra}_{\text{m}}(H) \in [1.6 \times 10^5 - 1.3 \times 10^6]$. We find that $h_{\text{SP}} / H \sim \text{Ra}_{\text{m}}^{1/3}$ and $\text{Nu} \sim \text{Ra}_{\text{m}}^{1/3}$ to within a negligible error. We conclude that for convection below a short SP for which the half-space cooling model applies, the scaling law $\text{Nu} \sim \text{Ra}_{\text{m}}^{1/3}$ remains valid even in the presence of viscous dissipation in the subduction interface.

470 6.2.2. Case 2: convection below a plate with a long travel time

We now assume that the travel time of the plate is sufficiently long (> 80 Myr) that thermal thickening has stopped by the time it reaches the trench.

The dependence of h_{SP} on Ra_m then breaks down and h_{SP}/H becomes a simple constant in the model, with h_{SP} always at its maximum value. Nevertheless,
 475 we assume that the amount of heat evacuated by the cell still corresponds to the heat lost during the thickening of the plate, while the amount of heat loss occurring after seafloor flattening occurs remains negligible. This implies that (21) continues to apply for our analysis.

Considering both contributions D_{SI} and D_{SP} to the viscous dissipation, we
 480 substitute (30) into (21) and obtain

$$\text{Nu} \sim \left[\text{Ra}_m \left(\frac{\ell}{L_z f_2(\theta)} \right) \frac{h_{\text{SP}}/H}{1 + \underbrace{\frac{\text{Ra}_m}{\text{Ra}_{\text{SP}}} \left(\frac{h_{\text{SP}}}{H} \right)^3 F(\theta) + \frac{\text{Ra}_m}{\text{Ra}_{\text{SI}}} \left(\frac{h_{\text{SP}}}{H} \right) \left(\frac{d_{\text{SI}}^2 C_V^2}{H^2 \sin(\theta_{\text{SI}}) f_2(\theta)} \right)}_{\hat{R}}} \right]^{1/2}, \quad (34)$$

where the bracket highlights the definition of \hat{R} . We now use (34) to determine the value of the exponent β that would appear in the corresponding $\text{Nu}-\text{Ra}_m^\beta$ relationship. Observing that $\text{Nu} = \text{Ra}_m^\beta$ implies $\beta = (\text{dNu}/\text{dRa}_m)(\text{Ra}_m/\text{Nu})$,
 485 we find that (34) implies

$$\beta = \frac{1/2}{1 + \hat{R}}. \quad (35)$$

Eq. (35) shows that β strongly depends on the dissipation partition coefficient \hat{R} . This relationship is particularly useful as it allows us directly to correlate \hat{R} with the present-day Urey ratio of the Earth, i.e. $\text{Ur} \approx (\tau_{\text{D}} - \tau_{\text{R}})/\tau_{\text{D}}$ (Labrosse
 490 & Jaupart, 2007). In the previous expression, $\tau_{\text{D}} \approx 3000$ Myr is the average decay time of the radioactive elements that generate heat in the Earth's interior. The time

$$\tau_{\text{R}} = \frac{MC_{\text{P}}T_0}{(1 + \beta + \beta n)Q_0} \quad (36)$$

is the relaxation time of mantle convection (Labrosse & Jaupart, 2007), where
 495 M is the mass of the Earth, C_{P} is an average heat capacity, n is the exponent of the Arrhenius law $\eta(T) = \eta_0(T/T_0)^{-n}$ describing the temperature dependence of the mantle viscosity and T_0 is the reference mantle temperature around which

is linearized the expression describing the rate of Earth's heat loss, whose corresponding reference value is Q_0 . Using the standard values for all the parameters appearing in (36) (Labrosse & Jaupart, 2007), we observe that for $\hat{R} = 0$ (no dissipation in the boundary layer), $\beta = 1/2$, $\tau_R \approx 530$ Myr and $Ur \approx 0.82$. By contrast, for $\hat{R} = 1$ (viscous dissipation equally partitioned between the boundary layer and the mantle), $\beta = 1/4$, $\tau_R \approx 1000$ Myr and $Ur \approx 0.66$. In order to satisfy the geochemical constraint $Ur \leq 0.5$, following the same reasoning, we need $\tau_R \geq 1500$ Myr and $\beta \leq 0.16$, which corresponds to $\hat{R} \geq 2$.

To conclude, we note that the models of Conrad & Hager (1999b) also lead to equation (35). In fact, starting from equation (5) of Conrad & Hager (1999b) and using their definition of the viscous dissipation in the mantle and the lithosphere, we recover exactly equation (35) after exploiting the relationship

$$\beta = (dNu/dRa_m)(Ra_m/Nu).$$

7. Influence of the lengthscales ℓ_b vs. \mathcal{R}_{\min} on dissipation partitioning

We now show how the estimates of the dissipation partitioning coefficient \hat{R} and the heat transport exponent β change dramatically depending on the length scale (ℓ_b or \mathcal{R}_{\min}) used to characterize the bending response of the SP.

515 We begin by defining

$$\alpha \equiv \frac{D_{\text{SP}}|_{\mathcal{R}_{\min}}}{D_{\text{SP}}|_{\ell_b}} = \left(\frac{\ell_b}{\mathcal{R}_{\min}} \right)^3 \quad (37)$$

as the factor by which D_{SP} is overestimated if \mathcal{R}_{\min} is adopted instead of ℓ_b , all else being equal. We estimate α in a realistic way by running time-dependent BEM simulations starting from the initial conditions reported in table 1. Next, 520 for both the ‘low viscosity contrast’ and ‘high viscosity contrast’ cases we stop the simulations at two characteristic depths $H_1/h_{\text{SP}} = \hat{H}_1 = 6.7$ and $H_2/h_{\text{SP}} = \hat{H}_2 = 10.0$. Owing to the quasi-stationarity of Stokes flow, these instantaneous configurations can be assumed to be representative for the purposes of our steady-state analysis.

525 Figure 7a shows that α increases rapidly as the slab progressively sinks, illustrating the strong influence of the chosen length scale in the evaluation of D_{SP} . For the two characteristic depths \hat{H}_1 and \hat{H}_2 , for example, we find $\alpha_1 = 33$ and $\alpha_2 = 134$ respectively when $\lambda_1 = 250$ (red empty circles), and $\alpha_1 = 16$ and $\alpha_2 = 51$ respectively when $\lambda_1 = 2500$ (black filled circles). The dependence of α 530 on the depth \hat{H} is explained by figure 7b, which shows the dimensionless lengths $\hat{\ell}_b$ and $\hat{\mathcal{R}}_{\min}$ as functions of \hat{H} for $\lambda_1 = 2500$. As the slab penetrates deeper, the bending length increases while the minimum radius of curvature tends to stabilize to a constant value. The ratio $\ell_b/\mathcal{R}_{\min}$, and thus the overestimate of the dissipation D_{SP} , therefore increases with the depth H . For $\lambda_1 = 250$, the 535 gap between the two curves of figure 7b becomes even wider, which is why α is larger for the ‘low viscosity contrast’ case (red empty circles, figure 7a).

To show how the overestimation of D_{SP} documented above influences the inferred value of β , we calculate the quantity

$$\hat{R}|_{\mathcal{R}_{\min}} = \left(\frac{\alpha + \delta}{1 + \delta} \right) \hat{R}|_{\ell_b}, \quad (38)$$

540 where α , $\delta \equiv D_{\text{SI}}/D_{\text{SP}}|_{\ell_b}$ and $\hat{R}|_{\ell_b}$ are determined from the BEM simulations.
 The corresponding values of β are then obtained from (35). The results are
 summarized in table 2 for our four characteristic combinations of \hat{H} and λ_1 . If
 we use \mathcal{R}_{min} as the bending length scale, the estimate of the boundary-layer
 dissipation D_{SP} is much higher, resulting in values of β close to zero in all cases.
 545 If, however, we adopt the correct length scale ℓ_b , $\beta \in [0.30, 0.34]$ for $\hat{H} = 6.7$
 and $\beta \in [0.25, 0.28]$ for $\hat{H} = 10$. This shows that one's assumption about the
 thickness of the convecting cell plays a role in the determination of β .

In light of table 2, we conclude that it is crucial to use the dynamic length
 scale ℓ_b rather than the purely geometric length \mathcal{R}_{min} to characterize the bending
 550 response of a viscous plate. We emphasize that even other purely geometric
 lengthscales, such as the product $\mathcal{R}_{\text{min}}\theta$ suggested by Capitanio et al. (2009),
 cannot capture the dynamic viscous response of the SP. This follows from the
 fact that viscous forces acting on a fluid volume do not define its shape, but
 rather the rate of change of that shape.

555 **8. Discussion**

Our results do not support previous proposals that the dissipation of energy associated with mantle convection is dominated by the contribution from stiff subduction zones (e.g. Conrad & Hager, 1999b; Becker et al., 1999). Adopting a modified version of the parameterized convection model of Conrad & Hager (1999b), we showed that a realistic treatment of plate bending implies small departures from the classical value of the heat transfer scaling exponent $\beta = 1/3$. Previous estimates of $\beta \approx 0$ might follow from overestimating the bending dissipation of the SP, as also suggested by Davies (2009). In particular, we showed how the bending response of the SP is strongly overestimated when it is described in terms of the minimum radius of curvature \mathcal{R}_{\min} , as done in many previous studies (e.g. Conrad & Hager, 1999b; Korenaga, 2003). At the same time, our results are broadly consistent with those of several other studies that have estimated the amount of energy dissipated in subduction zones (e.g. Capitanio et al., 2007; Krien & Fleitout, 2008; Leng & Zhong, 2010; Irvine & Schellart, 2012).

Our analysis, however, neglects certain aspects of real subduction systems and Earth’s mantle convection. We now discuss how these simplifications might affect our results.

We first consider the effect of a more realistic rheology involving both Newtonian diffusion creep and non-Newtonian power-law creep. The viscosity of a sheet having such a rheology and deforming by pure bending is

$$\eta = \left(\frac{1}{\eta_0} + \frac{1}{\eta_1} \right)^{-1}, \quad \eta_1 = BI^{1/n-1}, \quad (39)$$

where η_0 is a constant Newtonian viscosity, B is a constant rheological stiffness (units $\text{kg m}^{-1} \text{s}^{-2+1/n}$), and $I = (e_{ij}e_{ij}/2)^{1/2} \equiv |\dot{K}z|$ is the second invariant of the strain rate tensor. The fiber stress in the sheet is $\sigma_{ss} = -4\eta\dot{K}z$, and the bending moment is

$$M = \int_{-h/2}^{h/2} z\sigma_{ss}dz. \quad (40)$$

We are interested in the ratio Π of the bending moment $M_{\text{composite}}$ for a sheet with a composite rheology to the bending moment $M_{\text{Newtonian}} = -\eta_0 \dot{K} h^3 / 3$ of a purely Newtonian sheet. The integral (40) cannot be evaluated analytically
585 for arbitrary n , but can be integrated for particular choices of n . We therefore choose $n = 3$, a value close to that for olivine deforming by dislocation creep. We thereby find

$$\begin{aligned} \Pi(\lambda) &\equiv \frac{M_{\text{composite}}}{M_{\text{Newtonian}}} = -\frac{36 \cdot 2^{2/3}}{\lambda^4} + \frac{12}{\lambda^3} - \frac{18 \cdot 2^{1/3}}{5\lambda^2} + \frac{9 \cdot 2^{2/3}}{7\lambda} + \frac{72}{\lambda^{9/2}} \tan^{-1} \left(\frac{\lambda^{1/2}}{2^{1/3}} \right) \\ &= 1 - \frac{9}{11 \cdot 2^{2/3}} \lambda + O(\lambda^2), \end{aligned} \quad (41)$$

where $\lambda = (\eta_0/B)(|\dot{K}h)^{2/3}$ is a dimensionless number that vanishes in the limit of a purely Newtonian viscosity $\eta = \eta_0$. Eqn. (41) shows that Π is a monotonically decreasing function of λ with $\Pi(0) = 1$, $\Pi(1) = 0.663$ and $\Pi(10) = 0.168$. A sheet with composite rheology is therefore always weaker in bending than a purely Newtonian sheet. We conclude that subducting sheets with realistic composite rheology will contribute even less to the total viscous dissipation than
595 the $\approx 40\%$ predicted by our purely Newtonian models.

Next, we consider the influence of more realistic slab shapes. Tomographic images (e.g Goes et al., 2017) suggest that many slabs in natural subduction zones bend more tightly than our model predicts (figures 5a,c). Thus, we might expect real subduction zones to be characterized by shorter slabs and (consequently) shorter bending lengths. This argument implies a lower slope for the curve ℓ_b vs. \hat{H} in figure 7b (dashed curve). The difference between the bending dissipation calculated using ℓ_b vs. \mathcal{R}_{min} would then be lower for real subduction zones than in our model. However, due to the different natures and time evolutions of the two lengthscales, the overestimation factor α remains large.
605 For example, for the dashed curve in fig. 7b, we would obtain $\alpha \in [10 - 40]$ instead of our present model result $\alpha \in [16 - 51]$ (table 2, case $\lambda_1 = 2500$). Therefore, even if real subduction zones have shorter effective bending lengths

than our BEM models, we expect only a small variation in the range of β given in §7.

610 In closing, we remark that neither the parameterized convection model of §6 nor the BEM model considers the 660 Km discontinuity between the upper and lower mantle. Due to the viscosity jump at this depth, the SP experiences additional bending and stretching deformation that increases the amount of gravitational energy consumed. This additional source of energy dissipation
615 might considerably affect the $\text{Nu} \sim \text{Ra}_m^\beta$ heat transfer law.

9. Conclusion

In this work we studied the energetics of subduction using a numerical model based on the BEM. We endeavored to shed light on two topics: the partitioning of viscous dissipation among the different elements of a subduction zone (i.e. the subducting plate, the subduction interface and the mantle); and the influence of the energy dissipated in subduction zones on parameterized models of mantle convection.

By means of a scaling analysis of instantaneous BEM solutions for an isolated SP, we found that the ratio R of the energy dissipated in the upper boundary layer to the total energy dissipation obeys the scaling law $R \sim \text{St}/[\text{St} + F(\theta)]$, where St (the ‘flexural stiffness’) represents the SP’s mechanical resistance to bending and $F(\theta)$ is a function that accounts for the effect of the dip θ of the descending slab. Adding an OP to the system, we found that R also depends on a third parameter γ , the dimensionless strength of the subduction interface. Turning to unsteady subduction, we observed that the time evolution of $R(t)$ depends on the SP/mantle viscosity ratio λ_1 . Nonetheless, for both the ‘low viscosity contrast’ ($\lambda_1 = 250$) and ‘high viscosity contrast’ ($\lambda_1 = 2500$) cases explored, we observed that $R(t)$ never exceeds the value 0.5 corresponding to equipartition of the dissipation between the boundary layer and the mantle. We conclude that energy dissipation during free subduction is never dominated by the contributions of plate bending and interface shearing. We also found that the relative importance of dissipation in the subduction interface decreases as subduction proceeds.

Turning to the influence of strong subduction zones on mantle convection, we found that it primarily depends on the travel time of the lithosphere from the ridge to the trench. For short travel times ≤ 80 Ma, the thickness h_{SP} of the lithosphere when it enters the subduction zone is described by the classical half-space cooling model and depends on the mantle Rayleigh number Ra_m . The Nusselt number is then $\text{Nu} \sim \text{Ra}_m^\beta$ with $\beta = 1/3$, as for an isoviscous mantle. For long travel times, by contrast, h_{SP} is a constant. The heat transfer

scaling exponent is then $\beta = 0.5/(1 + \hat{R})$, where $\hat{R} \equiv R/(1 - R)$ is the ratio
 of the boundary-layer dissipation rate to that within the surrounding mantle.
 The partitioning factor \hat{R} depends strongly on the length scale one adopts to
 characterize the bending of the SP. If the minimum radius of curvature \mathcal{R}_{\min}
 650 of the plate is used, as in several previous studies, the bending dissipation of
 the SP is strongly overestimated and $\beta \rightarrow 0$. If however one uses the correct
 length scale, the ‘bending length’ ℓ_b , $\beta \in [0.30, 0.34]$ for $H/h_{\text{SP}} = 6.7$ and
 $\beta \in [0.25, 0.28]$ for $H/h_{\text{SP}} = 10$, where H is the depth of the convecting layer.
 Our overall conclusions are that strong subduction zones do not dominate the
 655 viscous dissipation associated with mantle convection, and that subduction zone
 dissipation leads to relatively small departures from the classical $\text{Nu} \sim \text{Ra}_m^{1/3}$
 heat transfer law.

10. Acknowledgments

This work has received funding from the European Union’s Horizon 2020 re-
660 search and innovation program under the Marie-Sklodowska-Curie grant agree-
ment No. 642029-ITN CREEP. It was supported in part by the French Pro-
gramme National de Planétologie (PNP) of CNRS/INSU, co-funded by CNES.
The authors thank A. Holt, F.A. Capitanio and an anonymous reviewer for con-
structive reviews that helped greatly to improve the manuscript. The CREEP
665 network is warmly thanked for inspiring and helpful discussions. All data and
methods necessary to understand, evaluate and replicate the reported research
are presented in the manuscript.

References

- 670 Becker, T. W., Faccenna, C., O'Connell, R. J., & Giardini, D. (1999). The
development of slabs in the upper mantle: Insights from numerical and lab-
oratory experiments. *Journal of Geophysical Research: Solid Earth*, *104*,
15207–15226.
- 675 Buffett, B., & Becker, T. (2012). Bending stress and dissipation in subducted
lithosphere. *Journal of Geophysical Research: Solid Earth*, *117*. doi:10.1029/
2012JB009205.
- Buffett, B., & Heuret, A. (2011). Curvature of subducted lithosphere from
earthquake locations in the Wadati-Benioff zone. *Geochemistry, Geophysics,*
Geosystems, *12*. doi:10.1029/2011GC003570.
- 680 Buffett, B. A. (2006). Plate force due to bending at subduction zones. *Journal*
of Geophysical Research: Solid Earth, *111*. doi:10.1029/2006JB004295.
- Capitanio, F., Morra, G., & Goes, S. (2007). Dynamic models of downgoing
plate-buoyancy driven subduction: Subduction motions and energy dissipa-
tion. *Earth and Planetary Science Letters*, *262*, 284–297.
- 685 Capitanio, F. A., Morra, G., & Goes, S. (2009). Dynamics of plate bending at
the trench and slab-plate coupling. *Geochemistry, Geophysics, Geosystems*,
10. doi:10.1029/2008GC002348.
- Christensen, U. R. (1985). Thermal evolution models for the Earth. *Journal of*
Geophysical Research: Solid Earth, *90*, 2995–3007.
- 690 Conrad, C. P., & Hager, B. H. (1999a). Effects of plate bending and fault
strength at subduction zones on plate dynamics. *Journal of Geophysical Re-*
search: Solid Earth, *104*, 17551–17571.
- Conrad, C. P., & Hager, B. H. (1999b). The thermal evolution of an Earth with
strong subduction zones. *Geophysical Research Letters*, *26*, 3041–3044.

- Davaille, A., & Limare, A. (2015). Laboratory studies of mantle convection.
695 *Treatise on Geophysics*, 7, 73–144.
- Davies, G. F. (2009). Effect of plate bending on the ury ratio and the thermal evolution of the mantle. *Earth and Planetary Science Letters*, 287, 513–518.
- Gerardi, G., & Ribe, N. M. (2018). Boundary element modeling of two-plate interaction at subduction zones: Scaling laws and application to the Aleutian
700 subduction zone. *Journal of Geophysical Research: Solid Earth*, 123, 5227–5248.
- Goes, S., Agrusta, R., Van Hunen, J., & Garel, F. (2017). Subduction-transition zone interaction: A review. *Geosphere*, 13, 644–664.
- Gurnis, M. (1989). A reassessment of the heat transport by variable viscosity
705 convection with plates and lids. *Geophysical Research Letters*, 16, 179–182.
- Holt, A. F., Buffett, B. A., & Becker, T. W. (2015). Overriding plate thickness control on subducting plate curvature. *Geophysical Research Letters*, 42, 3802–3810.
- Irvine, D., & Schellart, W. (2012). Effect of plate thickness on bending radius
710 and energy dissipation at the subduction zone hinge. *Journal of Geophysical Research: Solid Earth*, 117.
- Jaupart, C., Labrosse, S., Lucazeau, F., & Mareschal, J. (2015). Temperatures, Heat and Energy in the Mantle of the Earth. *Treatise on Geophysics*, 7, 223–270.
- 715 Jaupart, C., & Mareschal, J.-C. (2010). *Heat generation and transport in the Earth*. Cambridge university press.
- Korenaga, J. (2003). Energetics of mantle convection and the fate of fossil heat. *Geophysical Research Letters*, 30, 20–24.
- Krien, Y., & Fleitout, L. (2008). Gravity above subduction zones and forces
720 controlling plate motions. *Journal of Geophysical Research: Solid Earth*, 113.

- Labrosse, S., & Jaupart, C. (2007). Thermal evolution of the Earth: Secular changes and fluctuations of plate characteristics. *Earth and Planetary Science Letters*, *260*, 465–481.
- Leng, W., & Zhong, S. (2010). Constraints on viscous dissipation of plate bending from compressible mantle convection. *Earth and Planetary Science Letters*, *297*, 154–164.
- Manga, M., & Stone, H. (1993). Buoyancy-driven interactions between two deformable viscous drops. *Journal of Fluid Mechanics*, *256*, 647–683.
- Nataf, H., & Richter, F. (1982). Convection experiments in fluids with highly temperature-dependent viscosity and the thermal evolution of the planets. *Physics of the Earth and planetary interiors*, *29*, 320–329.
- Pozrikidis, C. (1992). *Boundary integral and singularity methods for linearized viscous flow*. Cambridge University Press.
- Ribe, N. (2001). Bending and stretching of thin viscous sheets. *Journal of Fluid Mechanics*, *433*, 135–160.
- Ribe, N. M. (2010). Bending mechanics and mode selection in free subduction: A thin-sheet analysis. *Geophysical Journal International*, *180*, 559–576.
- Rose, I., & Korenaga, J. (2011). Mantle rheology and the scaling of bending dissipation in plate tectonics. *Journal of Geophysical Research: Solid Earth*, *116*.
- Slater, J., Jaupart, C., & Galson, D. (1980). The heat flow through oceanic and continental crust and the heat loss of the Earth. *Reviews of Geophysics*, *18*, 269–311.
- Solomatov, V. (1995). Scaling of temperature-and stress-dependent viscosity convection. *Physics of Fluids*, *7*, 266–274.
- Stacey, F. D., & Davis, P. M. (2008). *Physics of the Earth*. Cambridge University Press.

Turcotte, D., & Schubert, G. (2014). *Geodynamics*. Cambridge University Press.

Table 1: Initial configurations of the models whose time evolutions are shown in figure 5.

	SP				OP			
	θ_0	$L_{\text{SP}}/h_{\text{SP}}$	ℓ/h_{SP}	λ_1	d_2/h_{SP}	$L_{\text{OP}}/h_{\text{SP}}$	$h_{\text{OP}}/h_{\text{SP}}$	λ_2
‘Low viscosity contrast’	30°	20	5	250	0.25	20	1	250
‘High viscosity contrast’	30°	20	5	2500	0.25	20	1	2500

Table 2: Values of the coefficient δ , the dissipation ratio $\hat{R}|_L$ and the corresponding exponent $\beta|_L$, where $L = \ell_b$ or \mathcal{R}_{\min} , for four combinations of values of \hat{H} and λ_1 .

\hat{H}	λ_1	δ	α	$\hat{R} _{\ell_b}$	$\hat{R} _{\mathcal{R}_{\min}}$	$\beta _{\ell_b}$	$\beta _{\mathcal{R}_{\min}}$
6.7	250	0.81	33	0.48	19	0.34	0.03
6.7	2500	0.52	16	0.67	11	0.30	0.04
10.0	250	0.49	134	0.81	90	0.28	≈ 0
10.0	2500	0.62	51	0.97	32	0.25	0.02

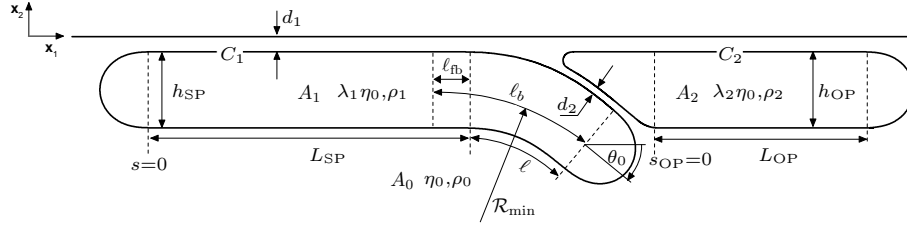


Figure 1: 2D model geometry. A dense subducting plate (SP) with viscosity $\eta_1 = \lambda_1 \eta_0$ and density ρ_1 sinks beneath an overriding plate (OP) with viscosity $\eta_2 = \lambda_2 \eta_0$ and density ρ_2 in an infinitely deep ambient fluid with viscosity η_0 and density ρ_0 . The dip angle at the end of the slab is θ_0 . The ambient fluid is bounded above by a free-slip surface $x_2=0$. The arclengths along the midsurfaces of the plates are $s \in [0, L_{\text{SP}} + \ell]$ for the SP and $s_{\text{OP}} \in [0, L_{\text{OP}}]$ for the OP. ℓ_b is the ‘bending length’, the length of the portion of the SP that deforms primarily by bending (Ribe, 2010). It is the sum of the slab length (ℓ) and the width of the zone of flexural bulging (ℓ_{fb}). The minimum radius of curvature of the plate’s midsurface \mathcal{R}_{min} is also shown.

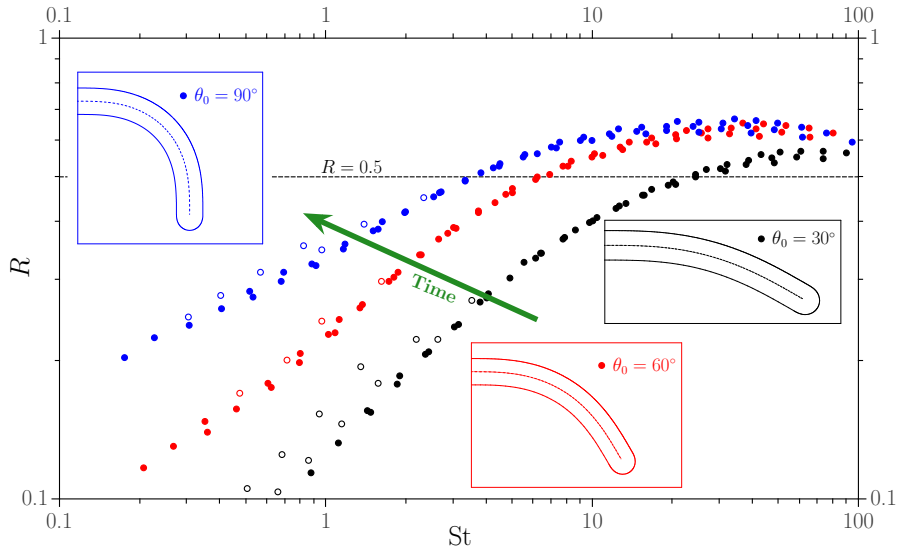


Figure 2: Dissipation ratio R as a function of the flexural stiffness St of the SP, predicted by BEM numerical solutions for $\lambda_1 \in [150 - 10^5]$, $\ell/h_{SP} \in [5 - 10]$, $L_{SP}/h_{SP} \in [20 - 32]$ and dip angles $\theta_0 = 30^\circ$ (black circles), 60° (red circles) and 90° (blue circles). The three insets show the geometry of the plate corresponding to each value of θ_0 . Empty circles indicate solutions for which dissipation by stretching of the plate is more than 5% of the total dissipation rate D_{SP} . The green arrow labelled ‘Time’ indicates the expected time evolution of the system.

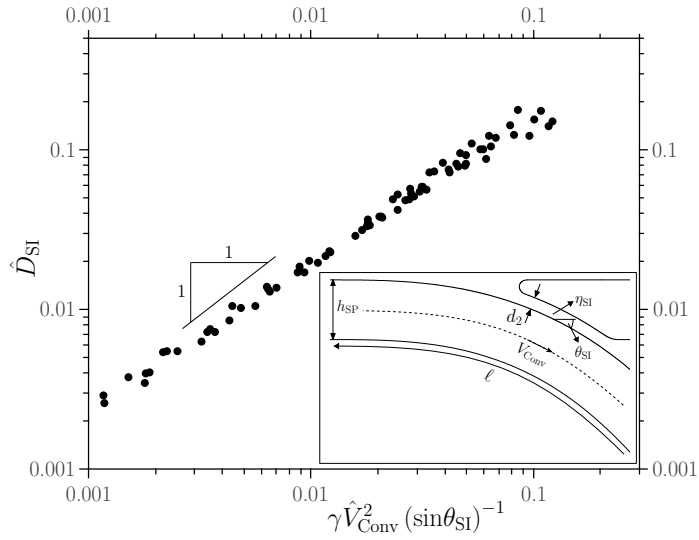


Figure 3: Dimensionless subduction interface dissipation rate D_{SI} as a function of the group of parameters on the right-hand side of eq. (17), for 108 BEM solutions with $\lambda_1 \in [150 - 10^5]$, $\lambda_2 = 250$, $\ell/h_{SP} \in [5 - 10]$, $L_{SP}/h_{SP} = L_{OP}/h_{OP} = 20$, $\gamma \in [2 - 6]$ and $\theta_0 = 60^\circ$. The range of γ used corresponds to that inferred by Gerardi & Ribe (2018) for the central Aleutian subduction zone. Different values of θ_0 shift the curve horizontally. Inset: close-up view of the subduction interface, defined by its thickness d_2 , inclination θ_{SI} and viscosity η_{SI} , where $\eta_{SI} \equiv \eta_0$ for our model. V_{Conv} is the convergence speed of the descending slab.

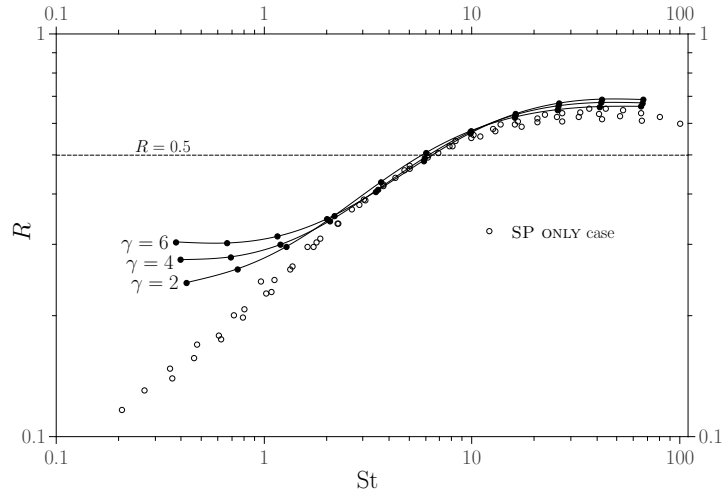


Figure 4: Dissipation ratio R as a function of the flexural stiffness St of the SP for three different values of γ . The BEM solutions for the SP+OP system were obtained for $\lambda_1 \in [150 - 10^5]$, $\gamma \in [2 - 6]$, $\ell/h_{SP} = 7$, $\theta_0 = 60^\circ$ and $L_{SP}/h_{SP} = L_{OP}/h_{OP} = 20$. Empty circles trace the corresponding curve for the SP ONLY case with $\theta_0 = 60^\circ$.

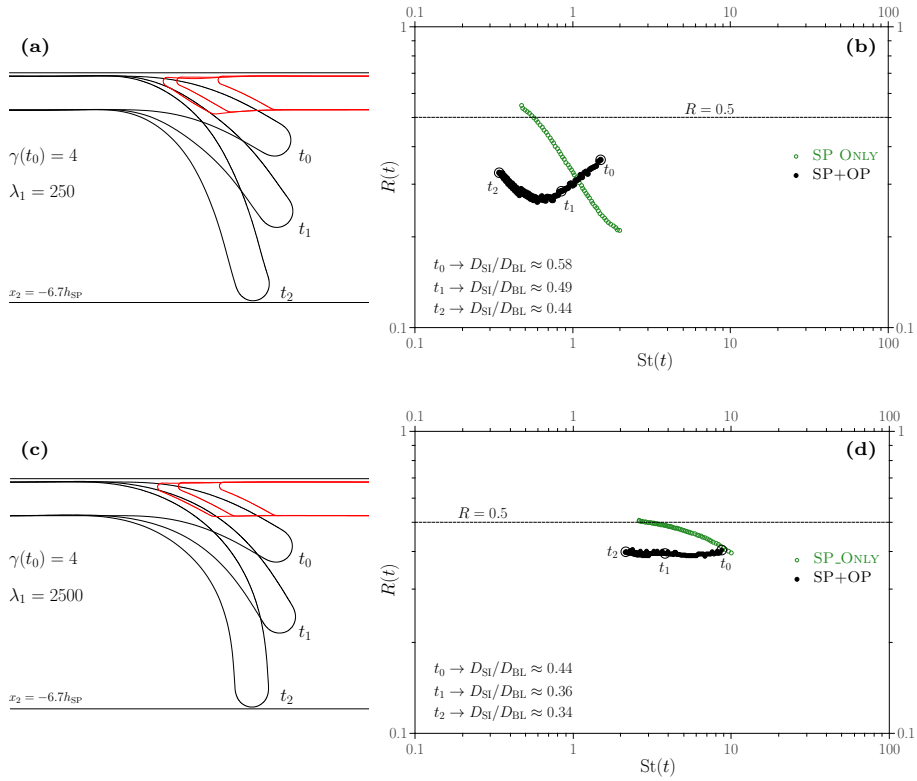


Figure 5: Unsteady subduction for two different viscosity ratios of the SP: $\lambda_1 = 250$ (top) and 2500 (bottom). The initial SI strength is $\gamma = 4$ for both cases. (a) and (c): system geometry (black line=SP, red line=OP) at three different times t_0 (the initial time), t_1 and t_2 , corresponding to the depths 210 km, 435 km and 660 km, respectively, where $d_1 = 0.1h_{SP}$ and $h_{SP} \approx 100$ km. (b) and (d): dissipation ratio R as a function of the time-varying flexural stiffness $St(t)$. Also reported is the value of the ratio D_{SI}/D_{BL} at the three times. For comparison, the green open circles show $R(St)$ for the same SP but without the OP. Time increases from right to left along these curves.

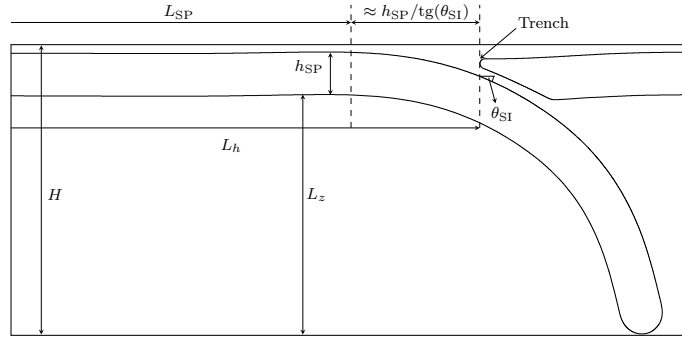


Figure 6: Geometrical representation of the convecting cell.

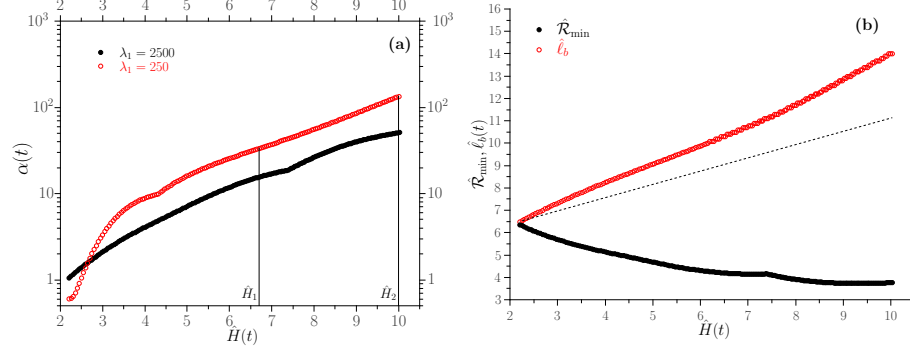


Figure 7: **(a)** Overestimation factor α as a function of the dimensionless cell thickness \hat{H} for viscosity ratios $\lambda_1 = 250$ (red open circles) and 2500 (black filled circles). Time increases from left to right. The intersections with the vertical straight lines give the values of α for the two characteristic depths \hat{H}_1 and \hat{H}_2 . **(b)** Time evolution of $\hat{\mathcal{R}}_{\min}$ (black filled circles) and $\hat{\ell}_b$ (red empty circles) for $\lambda_1 = 2500$. The dashed line represents the qualitative time evolution of ℓ_b that we can suppose representative of a more realistic subduction system (see § 8 for details). All lengths in the figures are given in units of the plate thickness.